

Atomic-scale modification of hybrid FePt cluster-assembled films

A. N. Dobrynin, D. N. Ievlev, G. Verschoren, J. Swerts, M. J. Van Bael, K. Temst, and P. Lievens*
Laboratorium voor Vaste-Stoffysica en Magnetisme, K.U.Leuven, Celestijnenlaan 200D, B-3001 Leuven, Belgium

E. Piscopiello and G. Van Tendeloo
Elektronenmicroscopie voor Materiaalonderzoek, Universiteit Antwerpen, Groenenborgerlaan 171, B-2020 Antwerp, Belgium

S. Q. Zhou and A. Vantomme
Instituut voor Kern- en Stralingsfysica, K.U.Leuven, Celestijnenlaan 200D, B-3001 Leuven, Belgium
 (Received 24 June 2005; revised manuscript received 25 January 2006; published 16 March 2006)

We present a study on the production of iron-platinum bimetallic clusters with a laser vaporization cluster source, and subsequent low-energy cluster beam deposition in ultrahigh-vacuum conditions. Time-of-flight mass spectrometry investigations of the clusters in the gas phase show that FePt is a stable alloy at the nanoscale. Magnetic and structural properties of the deposited 2.25 ± 0.5 nm cluster-assembled films with different Fe:Pt ratios are investigated with vibrating sample and superconducting quantum interference device magnetometry, Rutherford backscattering spectrometry, transmission electron microscopy, and x-ray diffraction. The as-deposited cluster films are highly porous and magnetically soft. A systematic study of the influence of annealing on the sample properties revealed that the chemically disordered-ordered phase transition only occurs in the cluster films with Fe:Pt ratio close to 1:1, and at temperatures higher than 500 °C. Combining magnetization and structural investigations we distinguish between the phase transition inside a single cluster and the coalescence of clusters, which starts to dominate at temperatures above 550 °C, leading to complete cluster intermixing on the atomic level.

DOI: [10.1103/PhysRevB.73.104421](https://doi.org/10.1103/PhysRevB.73.104421)

PACS number(s): 61.46.-w, 75.50.Tt, 75.50.Vv, 64.70.Nd

I. INTRODUCTION

Clusters containing a few hundred up to a few thousand atoms are uniquely suited for the study of magnetism at the nanometer scale because their size is comparable to the physical length scales relevant for magnetism, such as the exchange correlation length and the width of magnetic domain walls. Clusters or nanoparticles with a size smaller than 10 nm are single domain for all magnetic materials and they are superparamagnetic when noninteracting with each other.¹ At the same time crystal structures of clusters larger than 1 nm normally reflect their bulk counterparts, while a very large surface-to-volume ratio in clusters leads to a domination of surface (or interface) effects over volume effects.² This makes clusters especially attractive in the context of hybrid magnetic systems, e.g., exchange spring magnets,^{3,4} and exchange-biased systems.⁵ Clusters with high magnetic anisotropy also are considered as building blocks for high-density magnetic storage.¹

During the last few years iron-platinum (FePt) nanoparticles and nanocomposites were widely investigated mainly because of their potential applications in recording⁶⁻⁹ and high-performance permanent magnets.¹⁰⁻¹² The bulk FePt alloy can exist in two phases: chemically disordered face centered cubic (fcc), with Fe and Pt atoms randomly distributed over the crystal lattice, and chemically ordered face centered tetragonal (fct). The latter is obtained from the fcc structure by the formation of a superlattice of Pt atoms, which causes crystal lattice deformation due to the different atomic radii of Fe and Pt.^{6,13,14} The magnetocrystalline anisotropy is much higher for the ordered fct structure than for the disordered fcc one, leading to a high coercivity.¹³ The fcc-fct phase trans-

formation was observed at temperatures above 500 °C and for Fe:Pt compositions close to 1:1.^{6,15}

In this work we investigate the production of FePt clusters with a laser vaporization cluster source, and deposition of the clusters prepared in the gas phase by nondestructive low-energy cluster beam deposition.¹⁶⁻²⁰ The laser vaporization source operates in a highly nonequilibrium regime, which may lead to the formation of configurations that are not global energy minima. This was recently demonstrated for AuCu clusters,²⁰ where only a disordered phase (solid solution) was observed for all investigated cluster compositions, thus contradicting the results on nanoparticles produced by more conventional techniques (such as preparation in solution, etc.). Moreover, the used dual-target dual-laser vaporization source²¹ provides a very good handle on the cluster composition. This source also allows one to create “hybrid” systems by codeposition of clusters with different composition. The influence of the composition of the binary clusters on the magnetic and structural properties of the cluster-assembled films, the creation of hybrid magnetic cluster systems with different Fe:Pt ratios, and especially the evolution of the magnetic and structural properties of the hybrid samples with annealing are the focus of our work.

The cluster beam deposition technique for producing hybrid FePt nanocomposites is conceptually completely different from earlier employed chemical sintering^{11,12} and rapid Fe/Pt multilayer annealing¹⁰ approaches. As will be discussed, postannealing treatment of the as-deposited hybrid cluster films leads to complete intermixing on an atomic level of codeposited clusters with different compositions, thus yielding FePt nanocomposites with structures and magnetic properties different from those of films with similar

composition but obtained by other synthesis techniques.

II. IRON-PLATINUM CLUSTERS IN THE GAS PHASE

The FePt clusters are prepared in a dual-target dual-laser vaporization source, described in detail elsewhere.^{21–24} Iron and platinum targets are ablated independently by two *Q*-switched neodymium-doped yttrium aluminum garnet (Nd:YAG) lasers (532 nm, pulse width 7 ns). The produced plasma is injected into a cylindrical 3-mm-diameter source, where it is cooled with a 200 μ s pulse of high-purity He at pressures from 5 to 9 bar. The He is injected into the source with a pulsed supersonic gas valve (PSV, R. M. Jordan Company, Inc.) operated at a frequency of 10 Hz. At the end of the source there is a 0.8-mm-diameter outlet, followed by a conical nozzle (20 mm length, 0.35 sr solid angle) where the cluster beam is supersonically expanding. The cluster mass distribution is monitored with a reflectron-type time-of-flight (TOF) mass spectrometer, equipped with a dual-microchannel-plate (MCP) detector. By varying the source length (i.e., its volume), the delay time between the cooling gas and ablation laser pulses, and the He gas pressure, the cluster production regime can be tuned. In particular, an increase of the source volume up to certain limits leads to the production of larger clusters. The source length was changed in the range from 10 to 30 mm by installing nozzles with different extension parts. For the production of binary clusters the difference between the respective ablation laser delay times is crucial.

In Fig. 1(a) the mass spectra for Fe, Pt, and binary FePt clusters are shown. Fe and Pt targets were installed in the cluster source at a distance of 5 mm from each other, with the Pt target being closer to the nozzle, and the Fe target closer to the gas valve. The Fe target was ablated 350 μ s after the He gas pulse injection, and the Pt target 650 μ s. Since the mass peaks become broader with increasing cluster mass, neighboring peaks in the mass spectrum are overlapping for clusters with a large number of atoms. After integration of the MCP detector signal with a dc amplifier, this overlap results in a “hump” in the mass spectrum. For heavy elements, such as Pt, it is still possible to resolve individual peaks in the “hump,” whereas for the lighter elements, the peaks overlap completely. However, with respect to the number of atoms in clusters, the lighter elements may be resolved up to larger sizes than the heavier ones. Although losing information on the relative abundance of clusters with a different number of atoms, the hump gives direct information on the mass (and therefore size) distribution of the produced clusters. Since the amount of clusters of a certain mass is proportional to the area covered by the corresponding peak in the TOF spectrum,²⁴ the area under the hump is proportional to the amount of material in the clusters, contributing to the hump.

In Fig. 1(b) a zoomed-in region of small masses in the mixed FePt clusters mass spectrum is shown. Peaks corresponding to all possible combinations of Fe and Pt can be identified. Some peaks are degenerate due to the fact that the mass of seven Fe atoms is very close to the mass of two Pt

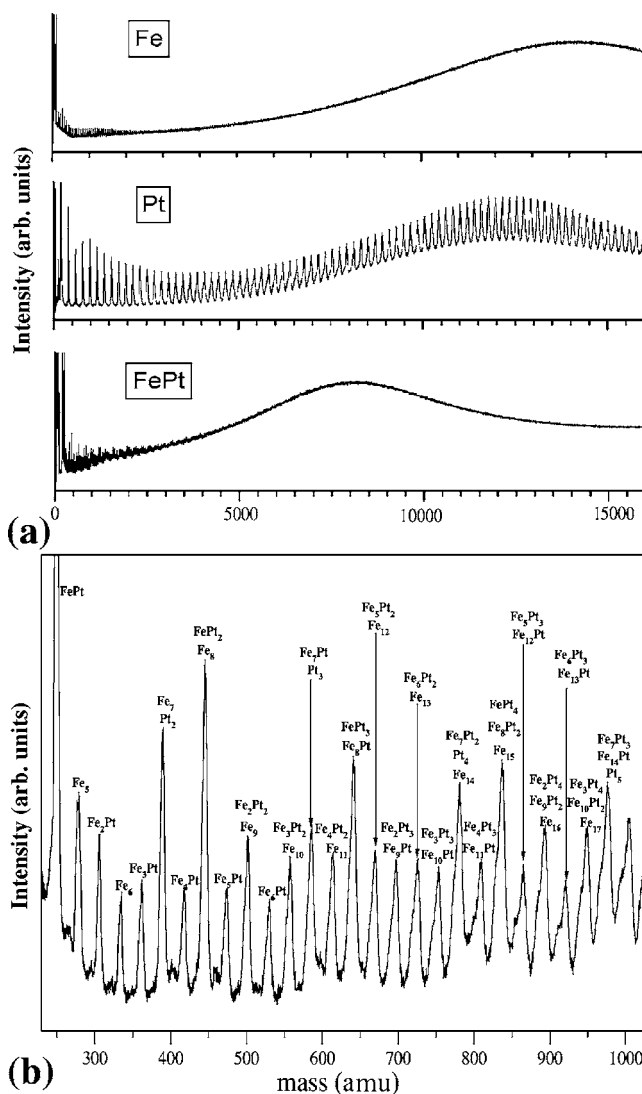


FIG. 1. (a) Time-of-flight mass spectra of Fe, Pt, and binary FePt clusters. (b) Zoomed in small-cluster region of the mixed FePt clusters.

atoms: $M(\text{Fe}_7) - M(\text{Pt}_2) = 0.759$ amu. The degenerate peaks are normally more abundant than those corresponding to the single clusters, since several clusters contribute to one peak. The observed perfect mixing of iron and platinum shows that FePt is a stable alloy at the nanoscale and many compositions may exist.

Figure 2(a) presents a typical mass spectrum for FePt clusters with the source parameters optimized for large cluster production (cluster source length 30 mm). The peak position at 35 000 amu corresponds to Fe clusters consisting of about 630 atoms, and to Pt clusters consisting of about 180 atoms. For mixed clusters with Fe:Pt ratio 1:1 there are about 280 atoms in one cluster. The cluster size can be estimated with the formula $d = 2R_W N^{1/3}$, where R_W is the Wigner-Seitz radius and N the number of atoms in the cluster.²⁴ For fcc FePt nanocrystals the lattice parameter is 0.376 nm,^{25,26} and $R_W = 0.148$ nm. The corresponding cluster size distribution is plotted in Fig. 2(b), and it shows that the cluster size is varying in the range 2.25 ± 0.5 nm. The small hump in the

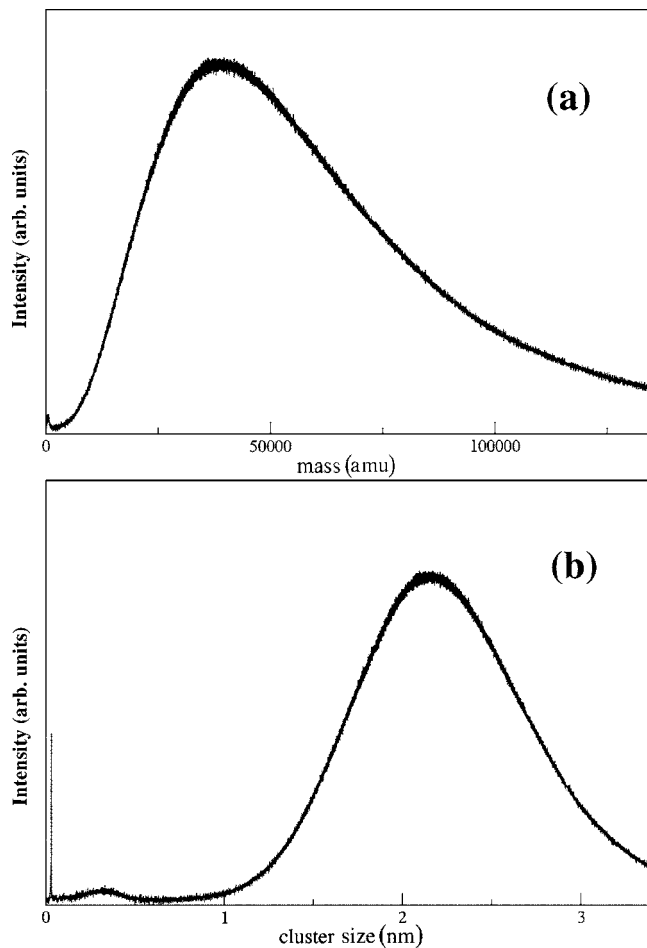


FIG. 2. (a) Typical TOF mass spectrum with the cluster source tuned for big-cluster production. (b) Corresponding size distribution.

beginning of the size distribution spectrum in Fig. 2(b) corresponds to a number of small clusters, the amount of which is negligible in comparison with the main hump contribution, since the area under the first one is less than 1% of the area under the big hump. The amount of material corresponding to the small hump is even more negligible, since it is proportional to the product of the number of clusters and the number of atoms in one cluster.

III. PRODUCTION AND STRUCTURAL CHARACTERIZATION OF CLUSTER-ASSEMBLED FILMS

The cluster films are grown in an ultrahigh-vacuum (UHV) cluster deposition chamber;²⁴ the background pressure is better than 10^{-9} mbar, while the pressure during the cluster source operation rises to about 10^{-7} mbar because of the influx of He gas. The cluster energies are determined by the He gas flow speed, which is about 500 m/s. This corresponds to energies from 0.07 eV/atom for pure Fe clusters, and to 0.25 eV/atom for pure Pt clusters. These energy values are typical for low-energy cluster deposition.^{2,17}

For the depositions we produced clusters using a single target with Fe:Pt ratios 1:1 (FePt) or 3:1 (Fe₃Pt). The cluster

source parameters were optimized for large-cluster production; the typical TOF mass and size distributions are shown in Fig. 2.

The clusters were deposited onto substrates held at room temperature. For the magnetic measurements substrates with a 700 nm amorphous SiO₂ layer on top of a 1 mm Si(100) single crystal were used. Four identical series of cluster films were produced, each including the following samples: FePt (using the FePt target), Fe₃Pt (using the Fe₃Pt target), and codeposited FePt and Fe₃Pt. The sample deposition sequence was the same for each series: first FePt and Fe₃Pt cluster production was optimized, then the FePt cluster film was deposited, followed by the Fe₃Pt and codeposited FePt and Fe₃Pt cluster films. The codeposition was performed by alternating the ablation of the two targets using a shutter for the ablating lasers, working at 0.1 Hz frequency (100 cluster pulses for each target). The deposition time was 2 h for each sample, resulting in 30-nm-thick (measured with atomic force microscopy) cluster films. Taking into account the mean cluster size of 2.25 nm, obtained from the TOF spectra, this deposition rate corresponds to the deposition of one cluster monolayer in 9 min. Therefore, with the used codeposition conditions (i.e., 10 s for each cluster beam), we do not end up with a layered cluster structure, but rather with a random mix of FePt and Fe₃Pt clusters. The mass distribution was regularly controlled during the depositions. A 10 nm capping layer of MgO was deposited on each cluster film in order to protect it from oxidation. MgO was evaporated from a Knudsen evaporation cell at 1800 °C; the deposition rates of the MgO and the cluster beam were controlled with a quartz crystal thickness monitor.

The composition of the samples was determined with Rutherford backscattering spectrometry, using a 1.57 MeV He⁺ beam. For the FePt cluster films the Fe:Pt ratio was about the same for all samples and this value is 1.38:1 (Fe₅₈Pt₄₂). For the Fe₃Pt films the Fe:Pt ratio was varying in the range from 3.38:1 (Fe₇₇Pt₂₃) to 3.87:1 (Fe₇₉Pt₂₁). Since these values are averages over all clusters, we will label the cluster films in accordance with the corresponding target compositions (FePt and Fe₃Pt) for the sake of brevity. The compositions of the mixed FePt-Fe₃Pt films were also determined and in each series this was close to a 1:1 ratio of the corresponding “FePt” and “Fe₃Pt” clusters.

In order to allow for a structural analysis of the films with transmission electron microscopy (TEM), samples were prepared in the following way: 10 nm of MgO was deposited onto a NaCl substrate, followed by a 15-nm-thick FePt cluster film, and a 10 nm MgO layer covering the film. Afterward the NaCl was dissolved in water and the “sandwich” structure MgO/FePt cluster film/MgO was caught on a TEM copper grid. The high-resolution TEM (HRTEM) plane image of this FePt cluster film is shown in Fig. 3. There are individual spherical clusters distinguishable, and the film is highly porous. The cluster sizes determined with TEM are between 1.5 and 3 nm, which correlates well with the TOF size distribution. This means that the deposition is not destructive for the clusters, and that they keep the size and shape preformed in the gas phase.²⁰

The inset of Fig. 3 shows a high-resolution image of a single cluster. A fast Fourier transformation (FFT) analysis of

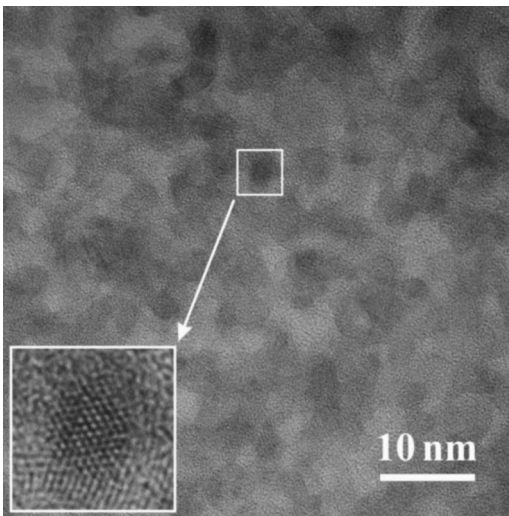


FIG. 3. Plane HRTEM image of the FePt cluster-assembled film. The inset shows a high-resolution TEM image of one FePt cluster, with fcc structure.

this image reveals the fcc structure of the cluster. The cross-sectional TEM images were obtained for one of the series of the samples on which the magnetization measurements were performed [Figs. 7(a), 7(c), and 7(e)]. For all samples (FePt, Fe₃Pt, and codeposited FePt-Fe₃Pt cluster films) the film morphology and the size distribution are similar.

IV. MAGNETIC PROPERTIES OF THE AS-DEPOSITED CLUSTER FILMS

Magnetization measurements were performed in plane with vibrating sample and superconducting quantum interference device (SQUID) magnetometers in the temperature range between 5 K and 300 K and at applied fields up to 40 kOe, and with magneto-optical Kerr effect (MOKE) magnetometry at 300 K. Measurements of the targets showed that the FePt is magnetically much harder than the Fe₃Pt target: for FePt the coercivity $H_c(300\text{ K})=1800\text{ Oe}$ and for the Fe₃Pt $H_c(300\text{ K})=50\text{ Oe}$, and these values are not strongly dependent on temperature. In Fig. 4(a) examples of magnetic hysteresis loops of Fe₃Pt, FePt, and codeposited FePt-Fe₃Pt cluster films are shown. These loops were taken with a SQUID at 300 K. The temperature dependences of the film coercivities are presented in Fig. 4(b). Coercivities of the FePt and Fe₃Pt cluster films are 40 and 30 Oe, respectively, at 300 K, and they are increasing with decreasing temperature. The H_c of the codeposited FePt-Fe₃Pt film is the highest (70 Oe at 300 K), and its temperature dependence is more pronounced. Similar results were obtained for all other series, the coercivities are varying in the range $\pm 10\text{ Oe}$ of the corresponding values for all samples of the considered series. The in-plane magnetization measurements by MOKE at different azimuthal angles did not reveal any anisotropy, confirming the random character of the cluster easy axis orientation.

The highly porous structure of the cluster-assembled films leads to specific magnetic properties, when the intercluster

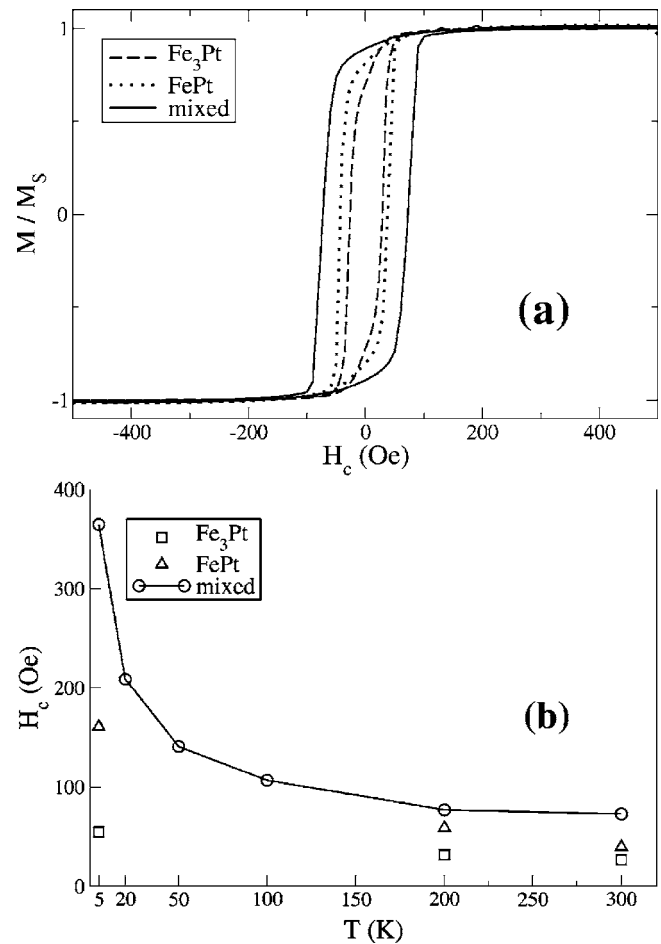


FIG. 4. (a) Magnetic hysteresis loops for Fe₃Pt, FePt, and FePt-Fe₃Pt mixed cluster films, taken at 300 K. The magnetization is normalized to the saturation value M_S for each sample. (b) Dependence of coercivity on temperature of the considered cluster films.

exchange interaction is much smaller than the intracluster exchange, and the magnetic domain is limited to one cluster.²⁷ If the cluster size is less than the exchange correlation length of the cluster material, then the cluster is single domain and all magnetic moments of the constituent atoms are collinear, forming a so-called “super-spin.”^{1,2} While the isolated single-domain magnetic particles may have a high coercivity at temperatures below the superparamagnetic blocking temperature,²⁸ the magnetic nanogranular assemblies are magnetically soft due to the intercluster exchange interaction, which increases the coherence of a magnetization rotation.²⁹ The random magnetic anisotropy axis orientation of the deposited clusters allows a description of the system with the random anisotropy (RA) model.^{30–33} While initially developed to describe amorphous magnetic materials,³² this approach was successfully implemented for the analysis of the magnetic behavior of cluster-assembled films.^{34–39} According to the RA model, the magnetic ground state in a cluster film is determined by the relative strength of an anisotropy field $H_r=2K_r/M_S$ and an exchange field $H_{ex}=2A/M_S R_a^2$.^{36,37} Here K_r is the anisotropy constant of the clusters, M_S the saturation magnetization, A the intergrain

exchange coupling constant, and R_a the cluster size. The ratio of the fields $\lambda_r = H_r/H_{ex}$ indicates whether the magnetic moments of the clusters are correlated at zero field or not. The correlated state of the cluster assembled film is called a correlated super spin glass (CSSG), and the magnetization vector is rotating throughout the sample with a characteristic length which is a factor of $1/\lambda_r^2$ larger than the cluster size. The CSSG state is easily destroyed by a small external field, which turns the system into the so-called “ferromagnet with wandering axes” (FWA) state.³⁷ This state is characterized by an approach to saturation following a $H^{-1/2}$ dependence in three dimensions. When the field reaches the crossover value $H_{co} = 2A/M_S R_a^2$, this dependence turns into the H^{-2} regime, typical for a system of noninteracting single-domain particles.⁴⁰ In order to verify the approach to saturation in our samples we performed a fit to the experimental data. In Fig. 5(a) this fit is shown for the Fe₃Pt sample. The full field range cannot be fitted with a single $H^{-1/2}$ or H^{-2} dependence. We were able, however, to fit the data with two parts, using an $H^{-1/2}$ dependence for fields ≤ 50 Oe, and an H^{-2} dependence for the fields ≥ 50 Oe. The fitting procedure in this case was as follows. At first, the data points in the range 400–500 Oe were fitted with the H^{-2} dependence and a correlation coefficient was obtained. Then one by one the data points with a lower field value were added to the fit range, and the data were fitted again with the same dependence. This was repeated until the correlation coefficient started to decrease. The rest of the data points were fitted to the $H^{-1/2}$ dependence. The crossover field thus obtained for the sample Fe₃Pt is 50 Oe. Taking into account the measured saturation magnetization value (about 3000 emu/cm³), we can estimate the intergrain exchange coupling constant $A = 5 \times 10^{-9}$ erg/cm. For the FePt sample we can fit the data in the same way, and the crossover field has the same value as for the Fe₃Pt sample [Fig. 5(b)]. For the mixed FePt-Fe₃Pt sample the whole data range is fitted by an H^{-2} law, showing that the intergrain exchange in this sample is negligible. In summary, the conducted analysis shows that the clusters in the considered samples very weakly interact one with each other, behaving rather as an isolated nanoparticles assembly.

It is noteworthy that there is not much difference in coercivities between the FePt and Fe₃Pt cluster films. This confirms that not the Fe:Pt composition but rather the alloy structure (which is fcc for both cluster films) plays a major role in the FePt nanoparticles magnetic behavior.

V. INFLUENCE OF ANNEALING ON MAGNETIC AND STRUCTURAL PROPERTIES

It was shown that thermal annealing may lead to a disordered-ordered (fcc-fct) phase transition in FePt nanoclusters in the gas phase,⁴¹ and in chemically sintered FePt nanoparticles.⁶ In the latter case isolated nanoparticles in the size range 3–10 nm were annealed at temperatures 450–600 °C, and x-ray diffraction (XRD) showed that the fcc-fct phase transformation started at temperatures between 450 and 500 °C. The phase transition gradually proceeded with increasing annealing temperature, and this was accompanied by a gradual increase of the nanoparticle coercivity.

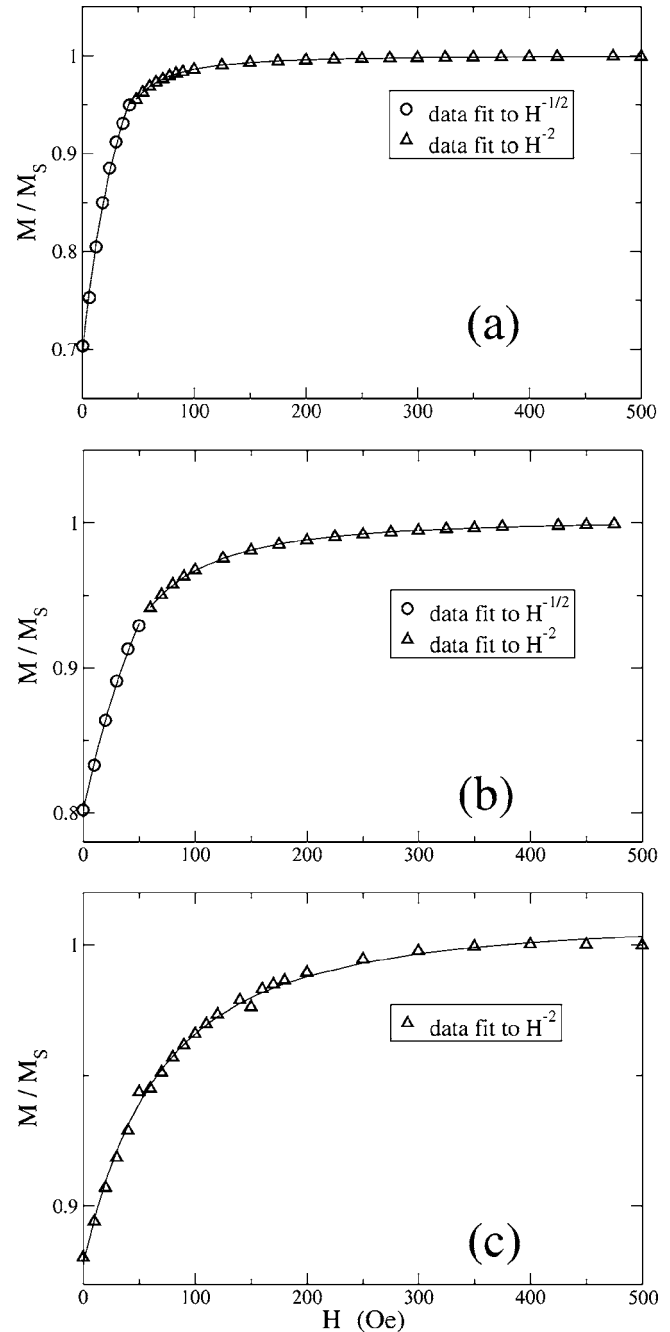


FIG. 5. Approach to saturation for Fe₃Pt (a), FePt (b), and FePt-Fe₃Pt (c) samples. The line shows a fit to the experimental data. For Fe₃Pt and FePt cluster films there are regions where the magnetization follows an $H^{-1/2}$ law (points marked with circles), showing the presence of weak intergrain exchange coupling. For the mixed FePt-Fe₃Pt cluster film the magnetization is fitted best with an H^{-2} law, showing that almost no intergrain exchange coupling exists.

The maximum coercivity value observed was 6.5 kOe after annealing of 4 nm Fe₅₂Pt₄₈ nanoparticle assemblies at 600 °C.

We investigated the influence of annealing on the magnetic and structural properties for one of the series of Fe₃Pt, FePt, and codeposited FePt-Fe₃Pt with 1:1 FePt:Fe₃Pt ratio

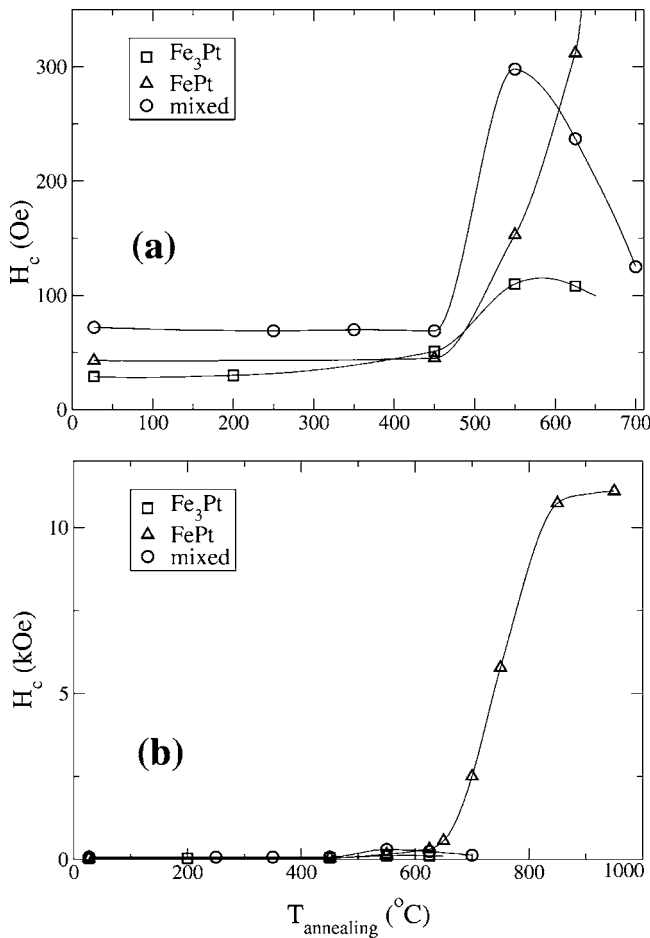


FIG. 6. Annealing influence on the room-temperature coercivities of Fe_3Pt (squares), FePt (triangles), and FePt- Fe_3Pt (circles) cluster films. (a) Zoomed in, (b) full range. Lines are a guide to the eye.

cluster films. The samples were annealed in the UHV deposition chamber ($p < 10^{-9}$ mbar) at different temperatures from 200 up to 950 °C. The annealing duration was 1 h for each temperature. The remanent magnetization was hardly (within $\pm 10\%$) influenced by the annealing. The dependences of the room-temperature H_c on the annealing temperature for the considered samples are presented in Figs. 6(a), zoomed in, and 6(b), full range. The coercivity of the FePt cluster films increases by a factor of 300 (up to 11 kOe) after annealing at 950 °C. For the Fe_3Pt and mixed FePt- Fe_3Pt samples the $H_c(T)$ dependences show peaks at 550 °C, but their coercivities drop again for higher annealing temperatures.

In Fig. 7 cross-sectional TEM images of the cluster films before and after annealing are given: Figs. 7(a) and 7(b) for FePt- Fe_3Pt as deposited and annealed at 550 °C, respectively; Figs. 7(c) and 7(d) for Fe_3Pt as deposited and annealed at 625 °C; Figs. 7(e) and 7(f) for FePt as deposited and annealed at 950 °C. The evolution of cluster coalescence with annealing temperature is visible when comparing Figs. 7(b), 7(d), and 7(e): while at 550 °C the coalescence is not very strong, at 625 °C this is dominating, and at 950 °C a densely packed structure of particles with grain sizes larger than 15 nm is formed.

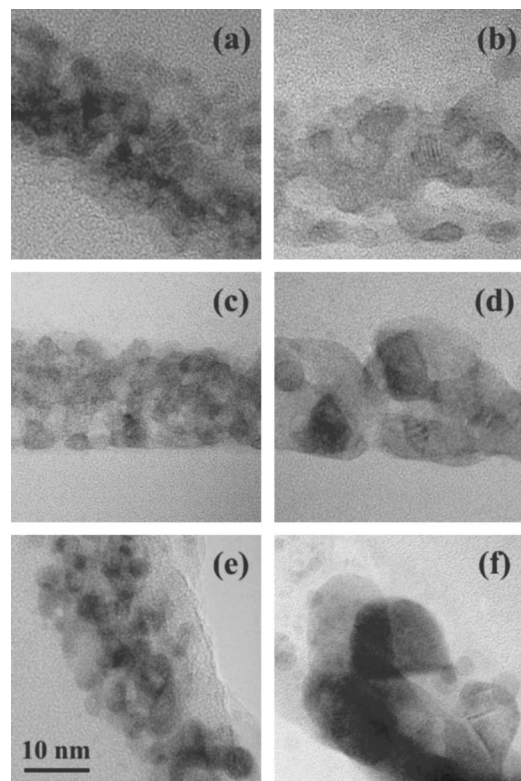


FIG. 7. TEM: cluster film annealing. (a) FePt- Fe_3Pt not annealed; (b) FePt- Fe_3Pt annealed at 550 °C; (c) Fe_3Pt not annealed; (d) Fe_3Pt annealed at 625 °C; (e) FePt not annealed; (f) FePt annealed at 950 °C.

In Fig. 8 the XRD spectra for the FePt cluster film before and after annealing at 600 °C are compared. For the as-deposited sample only the (111) diffraction peak is distinguished, which is very broad due to the small cluster size. In the spectrum for the annealed cluster film there are peaks appearing, forbidden for the fcc structure, but typical for a fct lattice: (110), (002), (210).^{6,42} For the Fe_3Pt sample there were no superstructure (fct) peaks found, either before or after annealing at 625 °C. Separate peaks for Fe or Pt are absent in all XRD spectra, demonstrating the formation of stable alloys of the two compounds.

The increase of coercivity with annealing of the FePt cluster films is consistent with the above described investigations,⁶ and corresponds to the fcc-fct phase transition, starting at 500 °C. This is also confirmed by the XRD spectrum taken after annealing at 600 °C, and showing peaks corresponding to the fct structure. The peak at 550 °C in the dependence of the coercivity on annealing temperature for the mixed FePt- Fe_3Pt cluster film [Fig. 6(a)] is appearing due to the fact that the fcc-fct phase transformation has started inside the FePt clusters, while the coalescence is not yet the dominating process [Fig. 7(b)]. At higher annealing temperatures the coalescence changes the composition of the alloy and the fct structure cannot be formed. For the FePt cluster films the coalescence does not change the film composition, and the fcc-fct transition continues until the coercivity reaches its plateau at 900–950 °C. The small peak in the dependence of coercivity versus annealing temperature

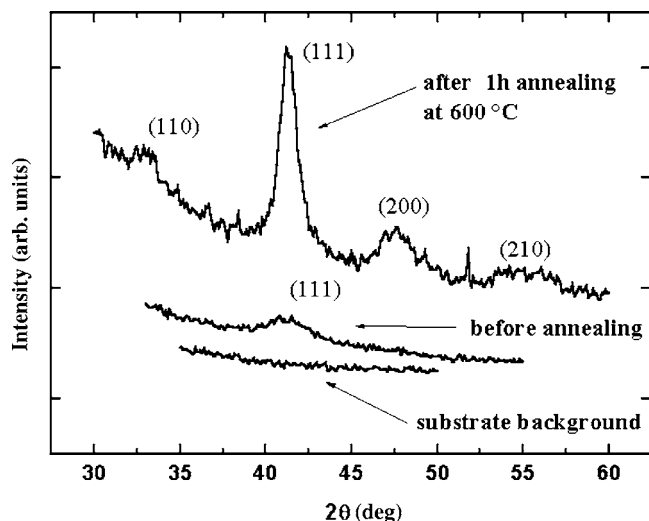


FIG. 8. XRD spectra of the as-deposited and annealed at 650 °C FePt cluster films. The diffraction peaks (110), (002), and (210), typical for the chemically ordered fct structure, appear in the annealed sample spectrum.

for the Fe₃Pt sample may be explained by the presence in this film of some clusters with an Fe:Pt ratio close to 1:1. In this case the peak origin is the same as for the mixed FePt-Fe₃Pt sample.

Thus by a combination of magnetization, TEM, and XRD measurements we can distinguish between the fcc-fct phase transition inside the FePt cluster (starting at 500 °C), and cluster coalescence (starting at 550 °C). Moreover, we show that the disordered-ordered phase transformation only occurs in the cluster film produced from the FePt target, while annealing of the Fe₃Pt cluster film leads to coalescence but not to changes of the crystal structure (e.g., magnetocrystalline anisotropy). The coalescence has a destructive influence on the codeposited FePt-Fe₃Pt cluster film, preventing the formation of an exchange spring magnet,^{10,12} consisting of magnetically hard fct FePt and magnetically soft fcc Fe₃Pt regions. In our case the local composition of the clusters is not preserved, and the fct structure cannot be formed after mixed film coalescence due to nonsuitable Fe:Pt composition.

VI. CONCLUSIONS

Binary iron-platinum clusters were produced in a dual-target, dual-laser vaporization source, and analyzed with time-of-flight mass spectrometry. By tuning the source parameters the cluster generation regime can be adjusted for producing small clusters, and relatively large ones, with suf-

ficiently narrow size distributions. Analysis of the TOF mass spectra of small FePt binary clusters shows that Fe and Pt are mixing easily with each other, forming all possible alloy combinations. This proves that FePt continues to be a good alloy at the nanoscale and many compositions may exist.

Nanogranular cluster-assembled films were grown by depositing clusters produced from FePt and Fe₃Pt targets with low kinetic energy. Characterization of the deposited cluster films with high-resolution transmission electron microscopy showed the highly porous structure of these films, and confirmed the size distribution obtained from the TOF mass spectra 2.25±0.5 nm. FFT analysis of the HRTEM images and XRD measurements of the as-deposited FePt and Fe₃Pt cluster films revealed the fcc crystal structure, which is known to be the chemically disordered phase of Fe_xPt_{1-x} alloys. The as-deposited cluster films are magnetically soft, but an intergrain exchange coupling obtained from an approach to saturation, is either very weak in FePt and Fe₃Pt samples, or negligible in mixed FePt-Fe₃Pt sample. Annealing of the cluster films leads to coalescence, starting at 550 °C. For cluster films produced of the FePt target the fcc-fct phase transition was identified with both magnetization and XRD measurements, and this is starting approximately at 500 °C. The coercivity of these samples reaches its saturation value of 11 kOe after annealing at 950 °C. For the Fe₃Pt sample no fcc-fct phase transition was observed and the sample stayed magnetically soft after annealing. For the codeposited FePt-Fe₃Pt cluster film there is a peak in the annealing temperature dependence of the coercivity at 550 °C, influenced by the ordering phase transition inside the FePt. Further annealing leads to cluster coalescence and the coercivity of the mixed samples drops back. This produces evidence of the atomic-level coalescence in FePt nanocluster films. This was only possible to perform by using a unique codeposition technique for production of hybrid FePt-Fe₃Pt cluster films, and characterizing the samples by three complementary techniques: magnetization measurements, x-ray diffraction, and high-resolution transmission electron microscopy.

ACKNOWLEDGMENTS

This work is supported by the Fund for Scientific Research, Flanders (FWO), the Flemish Concerted Action (Grant No. GOA/2004/02), the Belgian Interuniversity Poles of Attraction (Grant No. IAP/P5/01), and the European Community's Human Potential NanoCluster (Grant No. HPRN-CT-2002-00328) programs. M.J.V.B. is supported by the FWO.

*Electronic address: Peter.Lievens@fys.kuleuven.be

¹R. Skomski, *J. Phys.: Condens. Matter* **15**, R841 (2003).

²C. Binns, *Surf. Sci. Rep.* **44**, 1 (2001).

³E. Kneller and R. Hawig, *IEEE Trans. Magn.* **27**, 3588 (1991).

⁴R. Skomski and J. M. D. Coey, *Phys. Rev. B* **48**, 15812 (1993).

⁵A. N. Dobrynin, D. N. Ievlev, K. Temst, P. Lievens, J. Margueritat, J. Gonzalo, C. N. Afonso, S. Q. Zhou, A. Vantomme, E. Piscopiello, and G. Van Tendeloo, *Appl. Phys. Lett.* **87**, 012501 (2005).

⁶S. Sun, C. B. Murray, D. Weller, L. Folks, and A. Moser, *Science*

- 287**, 1989 (2000).
- ⁷B. Bian, D. E. Laughlin, K. Sato, and Y. Hirotsu, *J. Appl. Phys.* **67**, 6962 (2000).
- ⁸D. L. Peng, T. Hihara, and K. Sumiyama, *Appl. Phys. Lett.* **83**, 350 (2003).
- ⁹S. Stappert, B. Rellinghaus, M. Acet, and E. F. Wasserman, *J. Cryst. Growth* **252**, 440 (2003).
- ¹⁰J. P. Liu, C. P. Luo, Y. Liu, and D. J. Sellmyer, *Appl. Phys. Lett.* **72**, 483 (1998).
- ¹¹H. Zeng, S. Sun, T. S. Vedantam, J. P. Liu, Z. R. Dai, and Z. L. Wang, *Appl. Phys. Lett.* **80**, 2583 (2002).
- ¹²H. Zeng, J. Li, J. P. Liu, Z. L. Wang, and S. Sun, *Nature (London)* **420**, 395 (2002).
- ¹³R. A. Ristau, K. Barmak, L. H. Lewis, K. R. Coffey, and J. K. Howard, *J. Appl. Phys.* **86**, 4527 (1999).
- ¹⁴B. Stahl, J. Ellrich, R. Theissmann, M. Ghafari, S. Bhattacharya, H. Hahn, N. S. Gajbhiye, D. Kramer, R. N. Viswanath, J. Weissmüller, and H. Gleiter, *Phys. Rev. B* **67**, 014422 (2003).
- ¹⁵C. W. White, S. P. Withrow, J. D. Budai, L. A. Boather, K. D. Sorge, J. R. Thompson, K. S. Beaty, and A. Meldrum, *Nucl. Instrum. Methods Phys. Res. B* **191**, 437 (2002).
- ¹⁶H. Haberland, Z. Insepov, and M. Moseler, *Phys. Rev. B* **51**, 11061 (1995).
- ¹⁷A. Perez, P. Melinon, V. Dupuis, P. Jensen, B. Prevel, J. Tuailon, L. Bardotti, C. Maret, M. Treilleux, M. Broyer, M. Pellarin, J. L. Vaille, B. Palpant, and J. Lerme, *J. Phys. D* **30**, 709 (1997).
- ¹⁸C. Bréchnignac, Ph. Cahuzac, F. Carlier, M. de Frutos, A. Masson, C. Mory, C. Colliex, and B. Yoon, *Phys. Rev. B* **57**, R2084 (1998).
- ¹⁹P. Milani and S. Iannotta, *Cluster Beam Synthesis of Nanostructured Materials* (Springer, Berlin, 1999).
- ²⁰B. Pauwels, G. Van Tendeloo, E. Zhurkin, M. Hou, G. Verschoren, L. T. Kuhn, W. Bouwen, and P. Lievens, *Phys. Rev. B* **63**, 165406 (2001).
- ²¹W. Bouwen, P. Thoen, F. Vanhoutte, S. Bouckaert, F. Despa, H. Weidele, R. E. Silverans, and P. Lievens, *Rev. Sci. Instrum.* **71**, 54 (2000).
- ²²S. Neukermans, E. Janssens, H. Tanaka, R. E. Silverans, and P. Lievens, *Phys. Rev. Lett.* **90**, 033401 (2003).
- ²³E. Janssens, H. Tanaka, S. Neukermans, R. E. Silverans, and P. Lievens, *Phys. Rev. B* **69**, 085402 (2004).
- ²⁴N. Vandamme, E. Janssens, F. Vanhoutte, P. Lievens, and C. Van Haesendonck, *J. Phys.: Condens. Matter* **15**, S2983 (2003).
- ²⁵Z. R. Dai, S. Sun, and Z. L. Wang, *Nano Lett.* **1**, 443 (2001).
- ²⁶Z. R. Dai, S. Sun, and Z. L. Wang, *Surf. Sci.* **505**, 325 (2001).
- ²⁷J. F. Löffler, H. B. Braun, and W. Wagner, *Phys. Rev. Lett.* **85**, 1990 (2000).
- ²⁸W. Wernsdorfer, E. B. Orozco, K. Hasselbach, A. Benoit, B. Barbara, N. Demoncy, A. Loiseau, H. Pascard, and D. Mailly, *Phys. Rev. Lett.* **78**, 1791 (1997).
- ²⁹T. Schrefl, G. Hrkac, D. Suess, W. Scholz, and J. Fidler, *J. Appl. Phys.* **93**, 7041 (2003).
- ³⁰E. M. Chudnovsky and R. A. Serota, *Phys. Rev. B* **26**, R2697 (1982).
- ³¹E. M. Chudnovsky, W. M. Saslow, and R. A. Serota, *Phys. Rev. B* **33**, 251 (1986).
- ³²E. M. Chudnovsky, *J. Appl. Phys.* **64**, 5770 (1988).
- ³³E. M. Chudnovsky, *J. Magn. Magn. Mater.* **79**, 127 (1989).
- ³⁴L. Thomas, J. Tuailon, J. P. Perez, V. Dupuis, A. Perez, and B. Barbara, *J. Magn. Magn. Mater.* **140–144**, 437 (1995).
- ³⁵J. P. Perez, V. Dupuis, J. Tuailon, A. Perez, V. Paillard, P. Melinon, M. Treilleux, L. Thomas, B. Barbara, and B. Bouchet-Fabre, *J. Magn. Magn. Mater.* **145**, 74 (1995).
- ³⁶C. Binns, M. J. Maher, Q. A. Pankhurst, D. Kechrakos, and K. N. Trohidou, *Phys. Rev. B* **66**, 184413 (2002).
- ³⁷C. Binns and M. J. Maher, *New J. Phys.* **4**, 85 (2002).
- ³⁸S. A. Koch, G. Palasantzas, T. Vystavel, J. Th. M. De Hosson, C. Binns, and S. Louch, *Phys. Rev. B* **71**, 085410 (2005).
- ³⁹C. Binns, *Curr. Opin. Solid State Mater. Sci.* **8**, 203 (2004).
- ⁴⁰R. O'Handley, *Modern Magnetic Materials: Principles and Applications* (John Wiley & Sons, New York, 2000).
- ⁴¹B. Rellinghaus, S. Stappert, M. Acet, and E. F. Wasserman, *J. Magn. Magn. Mater.* **266**, 142 (2003).
- ⁴²C. Liu, T. J. Klemmer, N. Shukla, X. Wu, D. Weller, M. Tanase, and D. Laughlin, *J. Magn. Magn. Mater.* **266**, 96 (2003).